PHYSICAL REVIEW B **85**, 235438 (2012)

Prediction of solid-aqueous equilibria: Scheme to combine first-principles calculations of solids with experimental aqueous states

Kristin A. Persson,[1] Bryn Waldwick,[2] Predrag Lazic,[2] and Gerbrand Ceder[2]
[1]*Lawrence Berkeley National Laboratory, 1 Cyclotron Rd, Berkeley, California 94720, USA*
[2]*Massachusetts Institute of Technology, Cambridge, Massachusetts 02139, USA*

(Received 15 February 2012; published 20 June 2012)

We present an efficient scheme for combining *ab initio* calculated solid states with experimental aqueous states through a framework of consistent reference energies. Our work enables accurate prediction of phase stability and dissolution in equilibrium with water, which has many important application areas. We formally outline the thermodynamic principles of the scheme and show examples of successful applications of the proposed framework on (1) the evaluation of the water-splitting photocatalyst material Ta_3N_5 for aqueous stability, (2) the stability of small nanoparticle Pt in acid water, and (3) the prediction of particle morphology and facet stabilization of olivine $LiFePO_4$ as a function of aqueous conditions.

DOI: 10.1103/PhysRevB.85.235438 PACS number(s): 82.60.Lf, 82.20.Wt, 82.45.Bb, 82.45.Jn

I. INTRODUCTION

Ab initio computations of materials and their surfaces have largely focused on matter in vacuum. However, the influence of an environment (i.e., solution, atmosphere, etc.) can have a drastic effect on the properties of materials, thus influencing their performance under conditions relevant for their application area. Many materials-dependent processes, such as catalysis, energy storage, hydrothermal synthesis, dissolution, etc., motivate the development of a framework which accurately predicts solid-aqueous reaction energies and phase diagrams. While *ab initio* methods can relatively accurately predict bulk, nano, and surface properties, aqueous states remain a challenge. Direct simulations of aqueous states from first-principles Car-Parinello molecular dynamics have been performed for some species. These simulations obtain the structure, electronic state, and dynamics for the ions by assuming a solvation shell containing a fixed number (typically 30–50) of water molecules. To date, ions such as Li^+, Be^{2+}, Na^+, Mg^{2+}, Al^{3+}, K+, Ca^{2+}, Fe^{2+},Cu^{2+}, Ag^+, OH^-, $Al^{3+}(D_2O)_n$, and SO_3^- have been studied (see Refs. 1 and 2 and references therein). However, while encouraging, these calculations are nontrivial and too computationally demanding to be widely employed. Furthermore, they have mostly been applied to single-element aqueous ions, and many aqueous states form $AO_x^{\pm n}$ or $HAO_x^{\pm n}$ complexes. Using a hybrid scheme, Benedek *et al.*[3,4] have modeled proton-mediated dissolution of manganese and cobalt oxides in acid. In their calculation, experimental enthalpies of formation for the divalent metal ion (Mn^{2+} or Co^{2+}), the Li^+ and the H^+ aqeuous ions are referenced to the *ab initio* calculated free-atom energies of Mn, Co, Li, and H, respectively, to which tabulated empirically derived ionization and hydration energies were added. In a later work, Benedek *et al.*[5] recognized that the approximation for the exchange-correlation function contains significant errors for single molecules or atoms, which was remedied through an atomic-state correction factor. While computationally attractive, we note that this method relies on several approximations inherent in the use of assigned solvation shells and ionization energies.[6] Furthermore, the use of atomic species as intermediate reference states limits the applicability to single-species aqueous ions.

In this paper, we present a very simple scheme which enables us to directly combine *ab initio* calculated solids with experimental Gibbs free energies of arbitrary aqueous states. The method takes advantage of the fact that *formation* energies are essentially transferable between energy reference systems. However, the transferability is contingent on the level of accuracy of the calculation and on consistent reference states. Depending on the complexity of the electronic state of the material, *ab initio* solid formation energies can differ from their respective experimental counterparts by up to ± 0.5 eV/atom (see, for example, Ref. 7). Reaction energies in water are typically on the scale of hundreds of meV, which means that, for example, shifting a simple dissolution reaction by 200 meV/atom is equivalent to changing the pH by several units, which is unacceptable in a method striving for predictive power. The main concern thus becomes the consistency by which the reference states (the solid elements) and the compound formation energies are reproduced. Once a framework of internally coherent reference energies is obtained, the experimental aqueous and solid-state formation energies can be compared to each other in a meaningful way.

II. METHODOLOGY

In this section, we will systematically describe how to represent different species, i.e., the elements, compounds, aqueous ions, and liquid water within a framework of consistent reference energies so that these species can be compared to each other and solid-aqueous phase diagrams in equilibrium can be derived. For every species, we first outline how we obtain its Gibbs free energy and then how we define a species reference energy which is consistent with the rest of the framework. The organization of the species will follow an order of necessary "building blocks," i.e., we will start with solid and gaseous elements and work up to compounds, water, and lastly aqueous ions. All thermodynamic data in the paper are given for standard conditions of room temperature (RT) and 1 atm. However, we use T in the equations to keep the formalism as general as possible. All experimental thermodynamic data for solid states are taken from Ref. 8. For the aqueous states, we take experimental data primarily from Ref. 9 and, second, from Pourbaix's atlas.[10] As the data in Pourbaix's atlas are older, we only use it if a particular aqueous ion is not found in Ref. 9. All *ab initio* energies in the paper are obtained with the VASP (Ref. 11) implementation of density functional theory (DFT), using the Perdew-Burke-Ernzerhof generalized gradient approximation[12] (PBE GGA) description of the exchange-correlation energy. The projecter augmented wave (PAW) pseudopotential scheme[13] is used and the convergence of total energies with respect to plane-wave cutoff and k-point density is within 5 meV/atom. For all magnetic materials, ferromagnetic spin-polarized calculations are employed, which in some cases (e.g., the Mn-O system) introduce errors with respect to the ground-state energy. For very accurate low-temperature Pourbaix diagrams or for systems with strong magnetic coupling, we encourage the users of the formalism to carefully optimize their calculations for the ground-state magnetic configuration. Finally, when comparing energies between different compounds for which GGA and GGA + U (e.g., Mn and MnO) have been used, we employ the mixing scheme of Jain *et al.*[14]

A. Solid elements

We begin by considering the solid elements at moderate temperatures and normal pressure, i.e., close to standard state conditions. Elements that are solid can be well represented by DFT calculations. We therefore assign the enthalpy of the solid element i, at moderate temperatures T, as

$$h_i(T) = E_i^{\mathrm{DFT}}. \tag{1}$$

Furthermore, at moderate temperatures, the entropic contributions to the free energy of solid elements are small so we approximate

$$s_i(T) = 0, \tag{2}$$

which yields the Gibbs free energy of the solid element i as

$$g_i(T) = h_i(T) - Ts_i(T) = E_i^{\mathrm{DFT}}. \tag{3}$$

We now define the *reference state* of a solid element i as the *stable* state at standard state (denominated "0" for zero), as approximated by DFT calculations. Thus, the enthalpy of the element reference state is taken as

$$h_i^{\mathrm{ref}}(T) = \min E_i^{\mathrm{DFT},0}, \tag{4}$$

which yields

$$g_i^{\mathrm{ref}}(T) = h_i^{\mathrm{ref}}(T) - Ts_i^{\mathrm{ref}}(T) \approx E_i^{0,\mathrm{DFT}}, \tag{5}$$

$$\mu^{\mathrm{ref}}(T) = h_i^{\mathrm{ref}}(T) - Ts_i^{\mathrm{ref}}(T) \approx E_i^{0,\mathrm{DFT}}. \tag{6}$$

We note that the reference state is arbitrary, and is chosen for convenience and transparency. The chemical potential of the element i in any phase at standard conditions can now be defined as

$$\begin{aligned} \mu_i^0 &= g_i^0 - \mu_i^{\mathrm{ref}} && (7)\\ &= \left(h_i^0 - h_i^{\mathrm{ref}}\right) - T\left(s_i^0 - s_i^{\mathrm{ref}}\right) && (8)\\ &\approx \left(h_i^0 - \min E_i^{0,\mathrm{DFT}}\right). && (9) \end{aligned}$$

The Gibbs free energy of solid elements does not change appreciably within the range of moderate temperatures and pressures, and we therefore approximate the chemical potential of solid elements as constant. To illustrate the formalism for solid elements, we take a simple example of body-centered Li metal. Body-centered Li metal is the stable state of Li at standard state, i.e., the reference state, which means that the chemical potential of Li metal is given by

$$\mu_{\mathrm{Li}}^0 = \left(h_{\mathrm{Li(bcc)}}^0 - E_{\mathrm{Li(bcc)}}^{0,\mathrm{DFT}}\right) = 0. \tag{10}$$

Thus, we note that, so far, our formalism adheres to standard thermodynamic conventions at standard state.

B. Oxygen gas

In principle, Eq. (9) can be used exclusively with DFT energies for all elements, but in practice we want to make corrections for some states where DFT performs poorly. To obtain an accurate estimate of Gibbs free energy of elements that are gaseous in their stable state at standard state, we need to make corrections to the energy as calculated by DFT. For example, it is well known that standard DFT [i.e., local density approximation (LDA)/GGA] exhibits large errors in the binding energy of the O_2 molecule.[15,16] Therefore, for the oxygen elemental state in the gas phase, we use an energy in Eq. (9) that has been corrected for such errors by comparing the calculated and experimental formation enthalpies of simple non-transition-metal oxides[7] and which has been extensively tested (see, for example, Refs. 17 and 18 and references therein). We assign the enthalpy of oxygen gas at standard state as

$$h_{\mathrm{O}}^0 = E_{\mathrm{O}}^{0,\mathrm{DFT}} + \Delta E_{\mathrm{O}}^{\mathrm{correction}}. \tag{11}$$

Furthermore, the entropy of gaseous elements is not negligible at RT and we take the entropic contributions to the Gibbs free energy at standard state from experiments:[8]

$$\begin{aligned} g_{\mathrm{O}}^0 &= h_{\mathrm{O}}^0 - Ts_{\mathrm{O}}^{0,\mathrm{exp}} && (12)\\ &= E_{\mathrm{O}}^{0,\mathrm{DFT}} + \Delta E_{\mathrm{O}}^{\mathrm{correction}} - Ts_{\mathrm{O}}^{0,\mathrm{exp}}. && (13) \end{aligned}$$

We assign the reference state of oxygen to be the stable state of the element at standard state (i.e., gaseous), as calculated by DFT, and corrected for entropy and binding-energy errors:

$$\begin{aligned} h_{\mathrm{O}}^{\mathrm{ref}} &= E_{\mathrm{O}}^{0,\mathrm{DFT}} + \Delta E_{\mathrm{O}}^{\mathrm{correction}}, && (14)\\ \mu_{\mathrm{O}}^{\mathrm{ref}} &= h_{\mathrm{O}}^{\mathrm{ref}}(T) - Ts_{\mathrm{O}}^{\mathrm{ref}}(T) && (15)\\ &= E_{\mathrm{O}}^{0,\mathrm{DFT}} + \Delta E_{\mathrm{O}}^{\mathrm{correction}} - Ts_{\mathrm{O}}^{0,\mathrm{exp}}, && (16) \end{aligned}$$

which yields the the chemical potential of the reference state for oxygen as

$$\begin{aligned} \mu_{\mathrm{O}}^{\mathrm{ref}}(T) &= E_{\mathrm{O}}^{0,\mathrm{DFT}} + \Delta E_{\mathrm{O}}^{\mathrm{correction}} - Ts_{\mathrm{O}}^{0,\mathrm{exp}}(T) && (17)\\ &= -4.25 - 10.6 \times 10^{-4} T\,\mathrm{eV/O}, && (18) \end{aligned}$$

where $E_{\mathrm{O}}^{0,\mathrm{DFT}} + \Delta E_{\mathrm{O}}^{\mathrm{correction}} = -4.25$ eV/O is taken from Ref. 7 and the entropy $s_{\mathrm{O}}^{0,\mathrm{exp}}$ is taken from Ref. 8. For T = 298 K, we obtain

$$\mu_{\mathrm{O}}^{\mathrm{ref}}(T) = -4.25 - 0.317 = -4.57 \text{ eV/O}. \tag{19}$$

We can now calculate the chemical potential of oxygen gas at standard state as

$$\mu_{\mathrm{O}}^0 = \left(g_{\mathrm{O}}^0 - \mu_{\mathrm{O}}^{\mathrm{ref}}\right) = 0, \tag{20}$$

which complies with standard thermodynamic conventions. We note that the chemical potential of oxygen gas will change significantly as a function of the environment. Thus, as a function of temperature and oxygen partial pressure, the chemical potential of oxygen gas becomes

$$\mu_{\mathrm{O}} = \mu^0_{\mathrm{O}} + RT \ln p_{\mathrm{O}}. \tag{21}$$

C. Solid oxide compounds

Solid oxide compounds are treated similarly to solid elements. We assign the enthalpy of the compound as the energy calculated by DFT and neglect entropic contributions (valid for moderate temperatures). For a compound containing the elements $i = 1,\ldots,n$, we obtain

$$h_{i=1,\ldots,n}(T) = E^{\mathrm{DFT}}_{i=1,\ldots,n}, \tag{22}$$

$$s_{i=1,\ldots,n}(T) = 0, \tag{23}$$

which yields the Gibbs free energy of the solid compound containing elements $i = 1,\ldots,n$ as

$$g_{i=1,\ldots,n}(T) = h_{i=1,\ldots,n}(T) - T s_{i=1,\ldots,n}(T) = E^{\mathrm{DFT}}_{i=1,\ldots,n}. \tag{24}$$

Furthermore, using the reference states for the elements, we can calculate the chemical potential of a solid oxide compound at standard state as its formation free energy (Δg) containing elements $i = 1,\ldots,n$ as

$$\mu^0_{i=1,\ldots,n} \equiv \Delta g^0_{i=1,\ldots,n} = g^0_{i=1,\ldots,n} - \sum_{i=1}^{n} \mu^{\mathrm{ref}}_i. \tag{25}$$

As a simple example, we consider the solid $\mathrm{Li_2O}$ and calculate its chemical potential at standard state:

$$\begin{aligned}
\mu^0_{\mathrm{Li_2O}} &= E^{0,\mathrm{DFT}}_{\mathrm{Li_2O}} - 2\mu^{\mathrm{ref}}_{\mathrm{Li}} - \mu^{\mathrm{ref}}_{\mathrm{O}} && (26)\\
&= -14.31 - 2(-1.91) - (-4.57) && (27)\\
&= -5.92\ \mathrm{eV/Li_2O}, && (28)
\end{aligned}$$

where $E^{0,\mathrm{DFT}}_{\mathrm{Li_2O}} = -14.3$ eV/fu, $\mu^{\mathrm{ref}}_{\mathrm{Li}} = -1.91$ eV/atom calculated using DFT, and $\mu^{\mathrm{ref}}_{\mathrm{O}} = -4.57$ eV/O is the corrected oxygen energy from Sec. II B. Using this approach, we can now describe all solid elements, oxygen gas, and all solid oxides within the same energy reference framework. For comparison, the experimental Gibbs free energy at standard conditions for $\mathrm{Li_2O}$ is -5.82 eV/fu.[8]

D. Water

Up to this point, the formalism is parallel to what is derived in Ref. 7. We now continue to integrate the aqueous states into this framework. The next species we consider is water. In an aqueous environment, many chemical and electrochemical reactions are enabled by the breakdown, formation, or incorporation of water molecules. It is therefore exceptionally important that our scheme retains the accurate formation energy for water. To ensure this, we effectively define the formation Gibbs free energy of water at standard state as that given by experiments:

$$\begin{aligned}
\mu^0_{\mathrm{H_2O}} &\equiv \Delta g^{0,\exp}_{\mathrm{H_2O}} && (29)\\
&= \Delta h^{0,\exp}_{\mathrm{H_2O}}(T) - T\Delta s^{0,\exp}_{\mathrm{H_2O}}(T) && (30)\\
&= \Delta h^{0,\exp}_{\mathrm{H_2O}}(T) - T\left[s^{0,\exp}_{\mathrm{H_2O}}(T) - 2s^{0,\exp}_{\mathrm{H}}(T) - s^{0,\exp}_{\mathrm{O}}(T)\right]. && (31)
\end{aligned}$$

Explicitly, with experimental data taken from Ref. 8, we obtain the chemical potential of water at $T = 298$ K,

$$\begin{aligned}
\mu^0_{\mathrm{H_2O}} &= -2.96 + T[7.24 - 21.26 - 13.54] \times 10^{-4} && (32)\\
&= -2.46\ \mathrm{eV/H_2O}, && (33)
\end{aligned}$$

and as a function of temperature and water activity $a_{\mathrm{H_2O}}$,

$$\mu_{\mathrm{H_2O}} = \mu^0_{\mathrm{H_2O}} + RT \ln a_{\mathrm{H_2O}}. \tag{34}$$

In most applications, the activity of water is taken as one. This means that the chemical potential of $\mathrm{H_2O}$ is fixed at a given temperature, regardless of other ionic concentrations in the aqueous solution. However, at high ionic concentrations, for example, very acidic or alkaline conditions, corrections to the water activity may have to be made.

E. Hydrogen gas

In equilibrium with water, Eq. (29) has important implications on the energy of other species. In an aqueous environment, $\mathrm{O_2}$ and $\mathrm{H_2}$ in their gaseous states are in equilibrium with water through the reaction

$$\tfrac{1}{2}\mathrm{O}_{2(g)} + \mathrm{H}_{2(g)} \leftrightarrow \mathrm{H_2O}_{(l)}. \tag{35}$$

From Eq. (35), we can write the chemical potential of water at standard state as a function of the oxygen and hydrogen Gibbs free energies

$$\mu^0_{\mathrm{H_2O}} = \Delta g^0_{\mathrm{H_2O}} = g^0_{\mathrm{H_2O}} - g^0_{\mathrm{H_2}} - \tfrac{1}{2} g^0_{\mathrm{O_2}}. \tag{36}$$

We observe from Eq. (36) that the Gibbs free energies of hydrogen gas and oxygen gas are dependent on the chemical potential of water in the standard state. This implies that among $\mu^0_{\mathrm{H_2O}}$, $g^0_{\mathrm{H_2}}$, and $g^0_{\mathrm{O_2}}$, we only have two independent variables. Given the Gibbs free energy of oxygen gas derived in Eq. (18), we now derive a reference Gibbs free energy for hydrogen gas so that Eq. (36) reproduces the correct experimental Gibbs free formation energy of water $\Delta g^{0,\exp}_{\mathrm{H_2O}}$:

$$g^{\mathrm{ref}}_{\mathrm{H}} = \tfrac{1}{2}\left[g^0_{\mathrm{H_2O}} - \Delta g^{0,\exp}_{\mathrm{H_2O}} - \tfrac{1}{2} g^0_{\mathrm{O_2}}\right]. \tag{37}$$

To achieve consistency within our energy framework, we calculate the energy of a single water molecule by DFT methods. The sole purpose of this water energy is to obtain a Gibbs free energy for the hydrogen gas within the same framework (i.e., same pseudopotentials and "flavor" of DFT) as all other calculated species. For all other purposes, the chosen water formation Gibbs free energy as defined by Eq. (29) will be used. To the calculated water energy we add the experimental water entropy at standard conditions. We now define the reference state chemical potential of hydrogen gas at standard state as

$$\mu_{\mathrm{H}}^{\mathrm{ref}} = g_{\mathrm{H}}^{\mathrm{ref}} \tag{38}$$

$$= \tfrac{1}{2}\left[g_{\mathrm{H_2O}}^{0} - \mu_{\mathrm{O}}^{0} - \Delta g_{\mathrm{H_2O}}^{0,\mathrm{exp}}\right] \tag{39}$$

$$\approx \tfrac{1}{2}\left[E_{\mathrm{H_2O}}^{0,\mathrm{DFT}} - T s_{\mathrm{H_2O}}^{0} - \mu_{\mathrm{O}}^{0} - \mu_{\mathrm{H_2O}}^{\mathrm{ref}}\right]. \tag{40}$$

Using $E_{\mathrm{H_2O}}^{0,\mathrm{DFT}} = -14.7$ eV/H_2O, $s_{\mathrm{H_2O}}^{0} = 7.24 \times 10^{-4}$ eV/H_2O K, $\mu_{\mathrm{O}}^{0} = -4.57$ eV/O from Sec. II B, and $\mu_{\mathrm{H_2O}}^{0} = -2.46$ eV/H_2O from Sec. II D, we obtain at $T = 298$ K

$$\mu_{\mathrm{H}}^{\mathrm{ref}} = g_{\mathrm{H}}^{\mathrm{ref}} \tag{41}$$

$$= \tfrac{1}{2}[-14.7 + 0.216 - (-4.57) - (-2.46)] \tag{42}$$

$$= -3.73 \text{ eV/H}. \tag{43}$$

Similar to the other elements, we can calculate the chemical potential for hydrogen gas at standard state as

$$\mu_{\mathrm{H}}^{0} = \left(g_{\mathrm{H}}^{0} - \mu_{\mathrm{H}}^{\mathrm{ref}}\right) = 0 \tag{44}$$

and the chemical potential of hydrogen gas as a function of temperature, and hydrogen partial pressure can be obtained through

$$\mu_{\mathrm{H}} = \mu_{\mathrm{H}}^{0} + \tfrac{1}{2} RT \ln p_{\mathrm{H_2}}, \tag{45}$$

where $p_{\mathrm{H_2}}$ is the partial pressure of hydrogen gas.

We observe that we have chosen the hydrogen reference state deliberately to ensure (1) the correct experimental formation Gibbs free energy of water and (2) accurate oxidation enthalpies of formation through the carefully fitted oxygen-gas reference state. Thus, by construction, our framework will produce accurate solid-state oxidation reaction energies as well as accurate reaction energies involving liquid water. As we will see later, the application areas of interest motivate this choice. However, we emphasize that the accuracy of solid and/or gaseous pure *hydride* reaction formation energies (e.g., $2A + xH_2 \rightarrow 2AH_x$) is not automatically guaranteed.

F. Other elements

Other elements that are gaseous or molecularlike in their standard state, such as N, Cl, F, S, etc., also exhibit inherent errors in DFT and corrections should be made. The formation energies of these species are relatively easily corrected as none of them are connected to the water formation energy. Similarly to the treatment of oxygen gas, we suggest comparing the DFT reaction enthalpies for common binary systems to experimental results as shown in Ref. 7 and adding an average correction term to the DFT energy. In this way, we obtain the enthalpy of the gaseous element i as

$$h_i^{0} = E_i^{0,\mathrm{DFT}} + \Delta E_i^{\mathrm{correction}}. \tag{46}$$

Furthermore, we take the entropic contributions to the Gibbs free energy at standard state from experiments:[8]

$$g_i^{0} = h_i^{0} - T s_i^{0,\mathrm{exp}} \tag{47}$$

$$= E_i^{0,\mathrm{DFT}} + \Delta E_i^{\mathrm{correction}} - T s_i^{0,\mathrm{exp}}. \tag{48}$$

We assign the reference state of the gaseous element i to be the stable state of the element at standard state, as calculated by DFT, and corrected for entropy and binding energy errors:

$$h_i^{\mathrm{ref}} = E_i^{0,\mathrm{DFT}} + \Delta E_i^{\mathrm{correction}}, \tag{49}$$

$$\mu_i^{\mathrm{ref}} = h_i^{\mathrm{ref}}(T) - T s_i^{\mathrm{ref}}(T) \tag{50}$$

$$= E_i^{0,\mathrm{DFT}} + \Delta E_i^{\mathrm{correction}} - T s_i^{0,\mathrm{exp}}, \tag{51}$$

which yields the the chemical potential of the reference state for the element i as

$$\mu_i^{\mathrm{ref}}(T) = E_i^{0,\mathrm{DFT}} + \Delta E_i^{\mathrm{correction}} - T s_i^{\mathrm{exp}}(T) \tag{52}$$

and the chemical potential of the element i at standard state as

$$\mu_i^{0} = \left(g_i^{0} - \mu_i^{\mathrm{ref}}\right) = 0. \tag{53}$$

G. Aqueous ions

To represent the species present in water, we need to obtain reference states for the dissolved states, i.e., the aqueous ions. This will be done in the same energy framework as the solids and the gases. To accurately calculate aqueous ions directly with DFT is computationally challenging, as mentioned in Sec. I. In this section, we suggest a simple scheme of obtaining the reference Gibbs free energy for an aqueous ion by ensuring that *one* representative calculated binary solid dissolves with exactly the experimental dissolution energy. The basic idea behind this scheme is that, if we have a reference energy for an aqueous ion which reproduces the correct dissolution for one solid, then accurate DFT solid-solid energy differences ensure that all other solids dissolve accurately with respect to that ion. The choice of representative solid is not arbitrary. The better the solid is represented by DFT, the more transferable the reference aqueous energy becomes. We therefore prefer to choose simple chemical systems (primarily binaries with an uncomplicated electronic structure) as representative solids. For an aqueous ion i at standard state conditions (e.g., room temperature, atmospheric pressure, and 1 M concentration) using a representative solid s, we define the chemical potential as

$$\mu_{i(\mathrm{aq})}^{0} = \mu_{i(\mathrm{aq})}^{0,\mathrm{exp}} + \left[\Delta g_s^{0,\mathrm{DFT}} - \Delta g_s^{0,\mathrm{exp}}\right] \tag{54}$$

$$= \mu_{i(\mathrm{aq})}^{0,\mathrm{exp}} + \Delta \mu_s^{0,\mathrm{DFT-exp}}, \tag{55}$$

where $\Delta\mu_s^{\mathrm{DFT-exp}}$ denotes the formation Gibbs free-energy difference between the calculated reference solid and its experimental respective value. This correction term shifts the chemical potential of the aqueous ion so that, within our framework, the reference solid dissolves with the correct experimental dissolution energy, with respect to the aqueous ion in question.

To clarify how this works, we use the example of calculating the reference-state Gibbs free energy for the aqueous ion $\mathrm{Li}_{(\mathrm{aq})}^{+}$. We choose Li_2O as the representative solid s and, using the energies presented in Secs. II A and II B, calculate the representative solid chemical potential correction term in Eq. (55) as

$$\Delta\mu^{0,\mathrm{DFT-exp}}_{\mathrm{Li_2O}} = \tfrac{1}{2}\left[E^{0,\mathrm{DFT}}_{\mathrm{Li_2O}} - 2\mu^{\mathrm{ref}}_{\mathrm{Li}} - \mu^{\mathrm{ref}}_{\mathrm{O}} - \mu^{0,\mathrm{exp}}_{\mathrm{Li_2O}}\right] \tag{56}$$

$$= \tfrac{1}{2}[-14.31 - 2(-1.91) - (-4.57) - (-5.82)] \tag{57}$$

$$= \tfrac{1}{2}[-5.92 + 5.82] = -0.05\ \mathrm{eV/Li}. \tag{58}$$

We note that the difference between the calculated and the experimental formation energies is small for $\mathrm{Li_2O}$, which reflects the accuracy of DFT as well as the use of the corrected oxygen reference state in the calculation of the formation energy. Using the experimental Gibbs free energy for $\mathrm{Li^+_{(aq)}}$ from Ref. 9, we can now obtain the reference state for $\mathrm{Li^+_{(aq)}}$ within our framework:

$$\mu^{0}_{\mathrm{Li^+_{(aq)}}} = \mu^{0,\mathrm{exp}}_{\mathrm{Li^+_{(aq)}}} + \Delta\mu^{0,\mathrm{DFT-exp}}_{\mathrm{Li_2O}} \tag{59}$$

$$= -3.04 + (-0.05) = -3.09\ \mathrm{eV/Li^+_{(aq)}}. \tag{60}$$

Furthermore, we denote the chemical potential of the Li aqueous ion at any state as

$$\mu_{\mathrm{Li^+_{(aq)}}}(T) = \mu^{0}_{\mathrm{Li^+_{(aq)}}} + RT\ln[\mathrm{Li^+}] - RT\ln(10)\mathrm{pH}, \tag{61}$$

which takes into account the temperature, activity of $\mathrm{Li^+}$ ions, and the pH of the solution.

We now show that this scheme reproduces the correct dissolution energy of the chosen representative solid $\mathrm{Li_2O}$ into $\mathrm{Li^+_{(aq)}}$. The dissolution reaction is written as

$$\mathrm{Li_2O} + 2\mathrm{H^+} \rightarrow 2\mathrm{Li^+_{(aq)}} + \mathrm{H_2O}. \tag{62}$$

Using either all experimental (from Refs. 8 and 9) energies *or* our calculated $\mathrm{Li_2O}$ together with the derived reference energy for $\mathrm{Li^+_{(aq)}}$, we find the exact same Gibbs free reaction energy at standard state:

$$\Delta g^{0,\mathrm{exp}} = 2(-3.04) + (-2.46) - (-5.82) \tag{63}$$

$$= -1.52\ \mathrm{eV} \tag{64}$$

$$\Delta g^{0,\mathrm{DFT}} = 2(-3.09) + (-2.46) - (-5.92) \tag{65}$$

$$= -1.52\ \mathrm{eV}. \tag{66}$$

Thus, we observe that using the proposed framework, we reproduce the correct experimental dissolution energy for the reference solid. We also note that this result is enabled by the choice of correct and consistent energy reference states for water and the relevant gases and elements, which yield accurate formation energies. When calculating dissolution reaction energies for complex solids, surfaces, etc., the transferability of the scheme relies on accurate solid-solid DFT energy differences and cancelations of calculational errors between different solid compounds in similar chemistries. For example, using Eq. (61), we can calculate Li dissolution of any lithium-containing compound, in any structure (nanoparticle, surface, bulk, etc.). Inherent approximations in the calculations regarding magnetic and electronic states are transferred between the solid of interest and its binary reference states. Thus, errors that are common to both the compound of interest and the binary reference state will largely cancel in the prediction of dissolution through the construction above.

III. VALIDATION

Using the described methodology, we can calculate and benchmark bulk Pourbaix diagrams for the elements. Pourbaix diagrams[10] show the stable state of any element in water as a function of pH and potential applied. This benchmarking should be performed for all elements within a target chemical space before aqueous stability of higher-order compounds, surfaces, or nanostructures, etc., are investigated. For example, if we are investigating the aqueous solubility of nanometric compounds within the Ta-N chemical space, we should benchmark the bulk Pourbaix diagrams of Ta and N, respectively.

In the following, we will give examples of benchmarking and validation for the elements Mn, Zn, Ti, Ta, and N. For a specific element Pourbaix diagram, we will analyze the passivation regions, which are defined by the water conditions under which a solid phase is stable. The aqueous conditions as well as the phase sequence will be compared to Pourbaix's atlas and other available experimental information. The corrosion regions are defined by the aqueous conditions for which the stable predominant phase is either an aqueous ion or solvated gas phase. These regions will also be evaluated for agreement with experiment, although we note that the information of available species (but not their relative stability with respect to an arbitrary solid) is obtained from experiment sources.

In Table I, we show the experimental Gibbs free energies, the experimental and calculated enthalpies of formation for the chosen binary reference states for these elements, and the resulting referenced Gibbs free energies of the aqueous ions.

In Fig. 1(a), we show the calculated Pourbaix diagram for Mn, generated by our formalism. In comparison to the well-known experimental Mn Pourbaix diagram reproduced in Fig. 1(b), we observe that the passivation and corrosion regions agree exceptionally well with experiments. We also note that all aqueous states as well as the majority of the solid states in the experimental Pourbaix diagram are found at their appropriate conditions. Three differences are noted: (1) MnOOH is stable in the calculated diagram instead of $\mathrm{Mn_2O_3}$; (2) the small stability region of $\mathrm{Mn_3O_4}$ in experiments is not found in the calculated diagram (although $\mathrm{Mn_3O_4}$ is among the solid states included in the data set); and lastly (3) the stability region of $\mathrm{Mn(OH)_2}$ is slightly decreased in the calculated diagram. In the case of $\mathrm{Mn_2O_3}$, we believe that our calculated diagram gives

TABLE I. Chosen binary solid reference states and their experimental and calculated energies for the example elements Mn, Zn, Ti, Ta, and N.

Solid reference state	Experimental Gibbs free energy (Ref. 8) $\mu_s^{0,\mathrm{exp}}$ (eV/fu)	Calculated enthalpy $\mu_s^{0,\mathrm{DFT}}$ (eV/fu)	Formation energy difference $\Delta\mu_s^{0,\mathrm{DFT-exp}}$ (eV/fu)
MnO	− 3.528	− 3.676	0.148
ZnO	− 2.954	− 3.2631	0.309
$\mathrm{TiO_2}$	− 9.213	− 9.584	0.371
$\mathrm{Ta_2O_5}$	− 19.814	− 19.814[a]	0.000
$\mathrm{N_2O_5}$	− 0.997	− 3.016	2.019

[a] $\mathrm{Ta_2O_5}$ is the only known binary oxide in the Ta-O phase diagram, which means that employing the mixing scheme of Ref. 14 reproduces exactly the experimental formation energy of $\mathrm{Ta_2O_5}$.

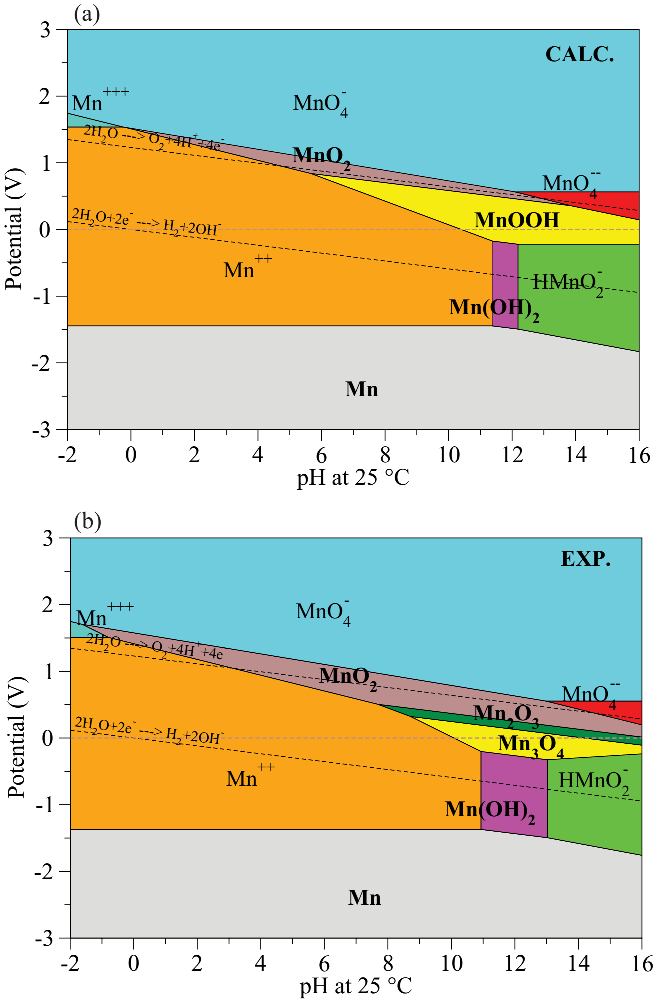

FIG. 1. (Color online) Mn Pourbaix diagrams generated using 10^{-6} M concentration for aqueous species at 25 °C. The diagram in (a) is calculated using the described formalism and (b) using only experimental data from Refs. 8–10.

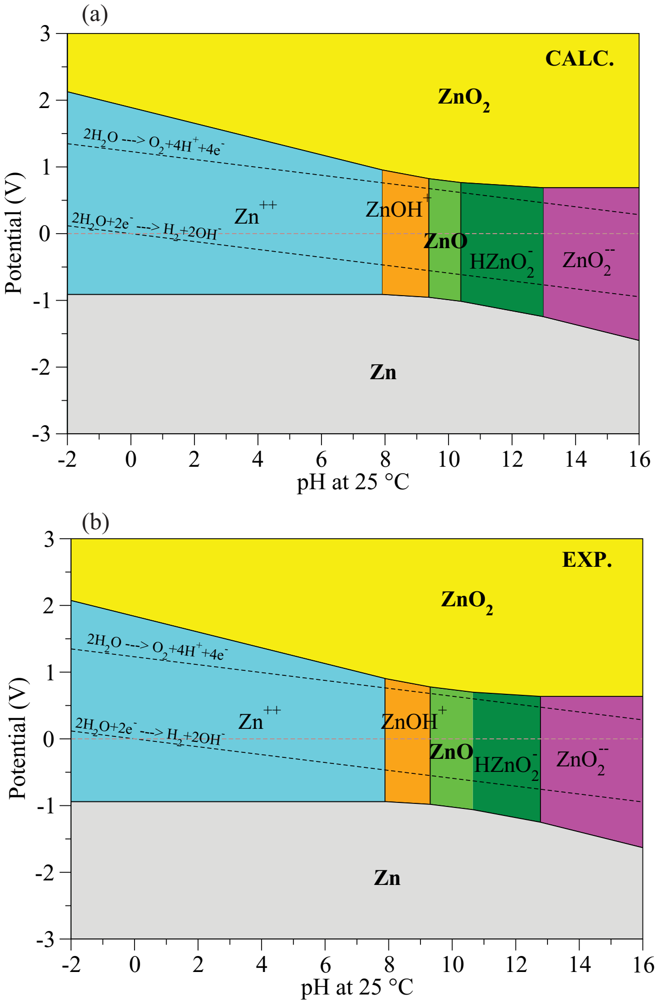

FIG. 2. (Color online) Zn Pourbaix diagrams generated using 10^{-6} M concentration for aqueous species at 25 °C. The diagram in (a) is calculated using the described formalism and (b) using only experimental data from Refs. 8–10.

the correct answer as MnOOH is not among the considered phases in the Pourbaix atlas[10] and MnOOH is consistently found at lower temperatures around pH = 11, and only converts to Mn_2O_3 at higher temperatures.[19] These findings suggest that MnOOH is indeed the ground state at lower temperature in an alkaline aqueous environment. In the case of Mn_3O_4, we find that the tie line created by MnOOH and $Mn(OH)_2$ corresponds to approximately 20 meV/fu lower energy than Mn_3O_4. This energy difference is within the accuracy of our calculations, as we have not fully optimized the magnetic and electronic structures of these solids. Thus, we would consider $Mn_3O_4$and MnOOH + $Mn(OH)_2$ equally stable in that region. The last noted difference between the calculated and experimental diagram is the slight underestimated stability of $Mn(OH)_2$, as the experimental diagram shows stability between $11 < \text{pH} < 13$, whereas the calculated diagram restricts the stability to $11.3 < \text{pH} < 12.3$.

Figure 2(a) shows another example of a calculated Pourbaix diagram for a transition metal: Zn. In this case, all solid- and aqueous-state stability regions are extraordinarily well represented by our methodology, compared to experimental results [see Fig. 2(b)]. In Fig. 3(a), we show the calculated Pourbaix diagram for Ti, generated by our formalism using solids calculated by first principles in the Ti-O/Ti-O-H composition space together with the aqueous ions from Table II. In comparison with the experimental Ti Pourbaix diagram[10] [cf. Fig. 3(b)], we observe that the passivation regimes as well as the corrosion regimes agree exceptionally well with experiments. Titanium metal and Ti oxides dissolve primarily to Ti^{2+} in the acid region. The very small stability region of aqeuous Ti^{3+} at very acid pH is also reproduced in the calculated diagram. In the passivation regime, a more detailed phase-diagram description of the solid stability is obtained from the calculations. We find additional slivers of stability regions for Ti_6O, Ti_3O, Ti_2O, Ti_4O_5, and Ti_3O_5 at reasonable conditions, which demonstrates the richness of Ti oxide phase space and its known stability in water. While only Ti, TiO, Ti_2O_3, and TiO_2 are presented in the original Ti Pourbaix diagram, we expect the additional phases shown in Fig. 3(a) to be stable from other reported discoveries and characterizations of Ti-O binary phases.[20–22]

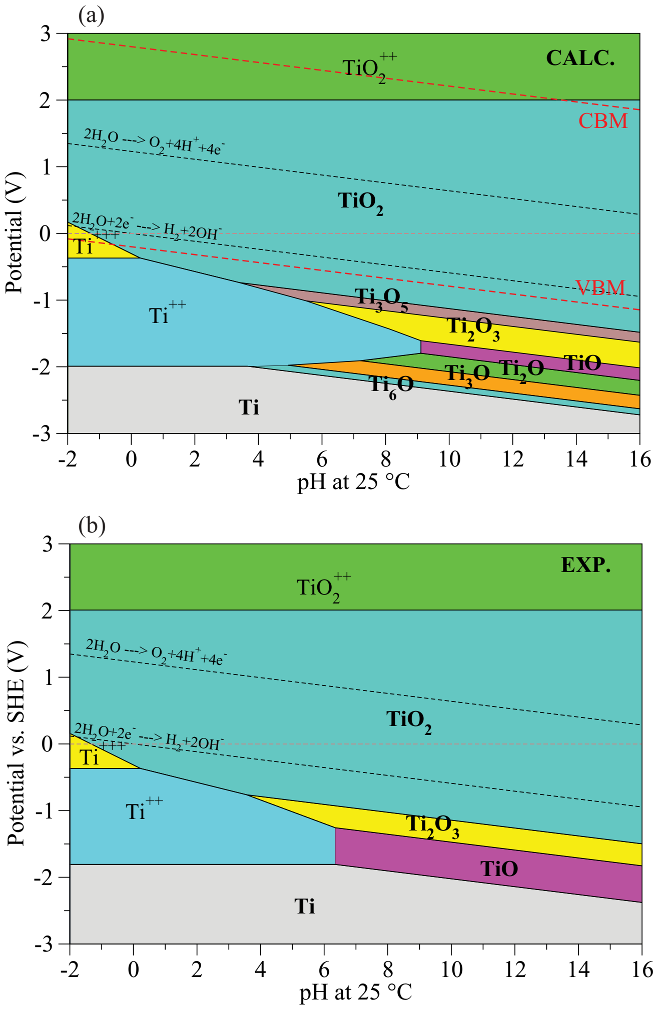

FIG. 3. (Color online) Ti Pourbaix diagrams generated using 10^{-6} M concentration for aqueous species at 25 °C. The diagram in (a) is calculated using the described formalism and (b) using only experimental data from Refs. 8–10.

TABLE II. Experimental and derived reference chemical potentials for known aqueous species for example elements Mn, Zn, Ti, Ta, and N.

Aqueous species	Experimental Gibbs free energy (Refs. 9 and 10) $\mu^{0,\mathrm{exp}}_{i(\mathrm{aq})}$ (eV/fu)	Referenced Chemical potential $\mu^{0}_{i(\mathrm{aq})}$ (eV/fu)
Mn^{2+}	−2.387	−2.535
MnO_4^{2-}	−5.222[a]	−5.370
$HMnO_2^-$	−5.243	−5.391
Mn^{3+}	−0.850[a]	−0.998
MnO_4^-	−4.658	−4.806
Zn^{2+}	−1.525	−1.466
$ZnO_{2(aq)}$	−2.921	−2.862
$ZnOH^+$	−3.518	−3.458
ZnO_2^{2-}	−4.042	−3.983
$HZnO_2^-$	−4.810[a]	−4.750
Ti^{2+}	−3.257[a]	−3.628
Ti^{3+}	−3.626[a]	−3.997
TiO^{2+}	−4.843[a]	−5.215
$HTiO_3^-$	−9.908[a]	−10.280
Zr^{4+}	−5.774	−5.907
ZrO^{2+}	−8.128	−8.261
$ZrOH^{3+}$	−8.250	−8.362
$ZrO_{2(aq)}$	−10.113	−10.245
$HZrO_2^{2+}$	−10.386	−10.518
$HZrO_3^{3-}$	−12.197	−12.329
$NH_{3(aq)}$	−0.277	−1.286
NH_4^+	−0.823	−1.832
NO_2^-	−0.334	−1.343
NO_3^-	−1.149	−2.158
$N_{2(aq)}$	0.188	−1.831
$N_2H_5^+$	0.854	−1.166
$N_2H_6^{2+}$	0.914	−1.105
$N_2O_2^{2-}$	1.438	−0.581
NH_4OH	−2.734[a]	−3.744
HNO_3	−1.146[a]	−2.156

[a]Data taken from Ref. 10.

We show the calculated Ta Pourbaix diagram in Fig. 4(a). Tantalum only exhibits two stable phases, Ta and Ta_2O_5, in agreement with experimental results in Fig. 4(b). Indeed, Ta is known to be almost completely insoluble under aqueous conditions, unless it complexes with halides such as F.[23]

Lastly, in Fig. 5(a), we show the calculated Pourbaix diagram for N, where the solid reference state is the solid state N_2O_5 (dinitrogen pentaoxide), as given in Table I. Pourbaix's atlas[10] does not have any data for solid N_2O_5, which is a known molecular solid that decomposes into a similarly structured gas at 32 °C.[24] From Table I, we observe that the calculated formation energy for N_2O_5 exhibits a large error compared to the experimental value. The relaxed structure of N_2O_5 was found to be quite similar to that reported by experiments, which leads us to speculate that the discrepancy between the formation energies is due to a poor representation within the GGA of the molecular bonding in solid N_2O_5. Following the formalism, we correct for this discrepancy between the experimental and calculated formation energies of N_2O_5, and the stability region shown in Fig. 5(a) [which also replaces the liquid HNO_3 region shown in Pourbaix's diagram, see Fig. 5(b)] is thus likely to be real, although we could still be missing aqueous phases that compete with the solid. Otherwise most features of the experimental N Pourbaix diagram are reproduced by our formalism. The dissolved gas NH_3 replaces the dissolved species NH_4OH at low potential alkaline conditions in the calculated diagram, but this is due to a slightly more stable (0.1 eV/fu) reference energy for NH_3 given by Ref. 9 as compared to Ref. 10, which pushes the reaction $NH_4OH \rightarrow NH_3 + H_2O$ towards the right-hand products.

IV. EXAMPLE APPLICATIONS

In the following section, we will show some examples of how the scheme outlined in Sec. II can be applied to different research problems of technological interest. We give examples relevant for evaluating stability of water-splitting photocatalysts, predicting dissolution of nanometric catalytic materials for low-temperature fuel cells, and guiding particle

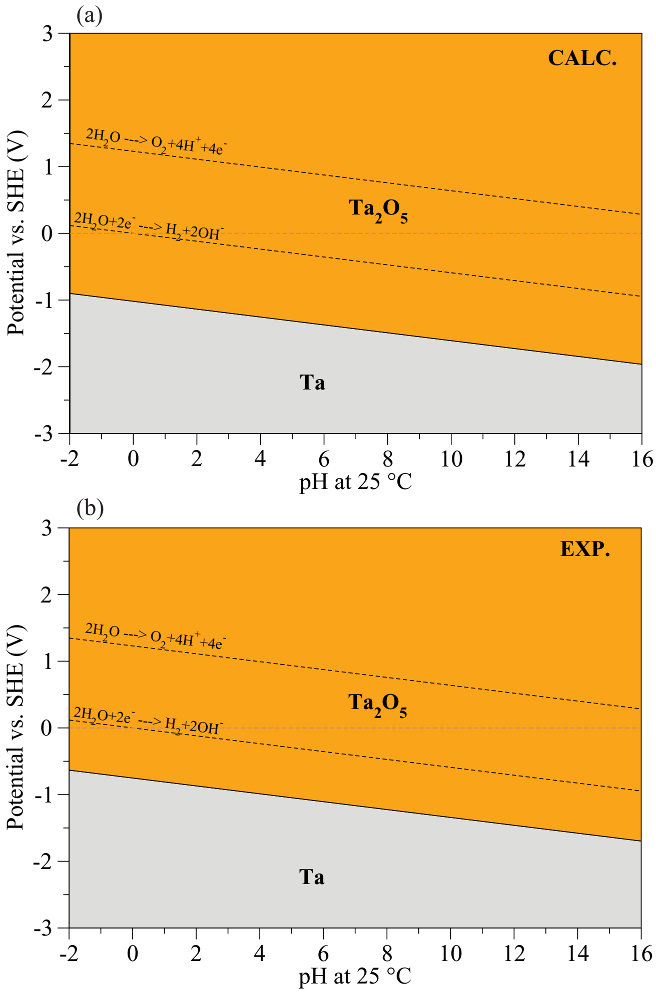

FIG. 4. (Color online) Ta Pourbaix diagrams generated using 10^{-6} M concentration for aqueous species at 25 °C. The diagram in (a) is calculated using the described formalism and (b) using only experimental data from Refs. 8–10.

morphology as a function of water conditions for hydrothermal synthesis.

A. Aqueous stability of photocatalytic materials

Photocatalysis uses the energy of the Sun to split water into oxygen and hydrogen, which enables a source of hydrogen for fuel cells. There are several key properties required for optimal photocatalytic materials, foremost among them having highly efficient absorption of visible light and absolute conduction-band minimum (CBM) and valence-band maximum (VBM) that enable thermodynamically favorable oxygen and hydrogen evolution reactions in water. The material should also remain long-term stable under operating conditions in the aqueous electrolyte, which tends to be highly corrosive. Today, the most commonly used materials are oxides, largely because of their known stability in water. However, oxides tend to exhibit deep valence-band positions (O_{2p} orbitals) resulting in band gaps that are too large to absorb visible light efficiently. In contrast, metal nitrides or oxynitrides present interesting candidates as the N_{2p} orbital has a higher potential energy than the O_{2p} orbital. Unfortunately, nitrides are generally less stable in water than oxides, which causes a subtle tradeoff between increased efficiency and aqueous stability.

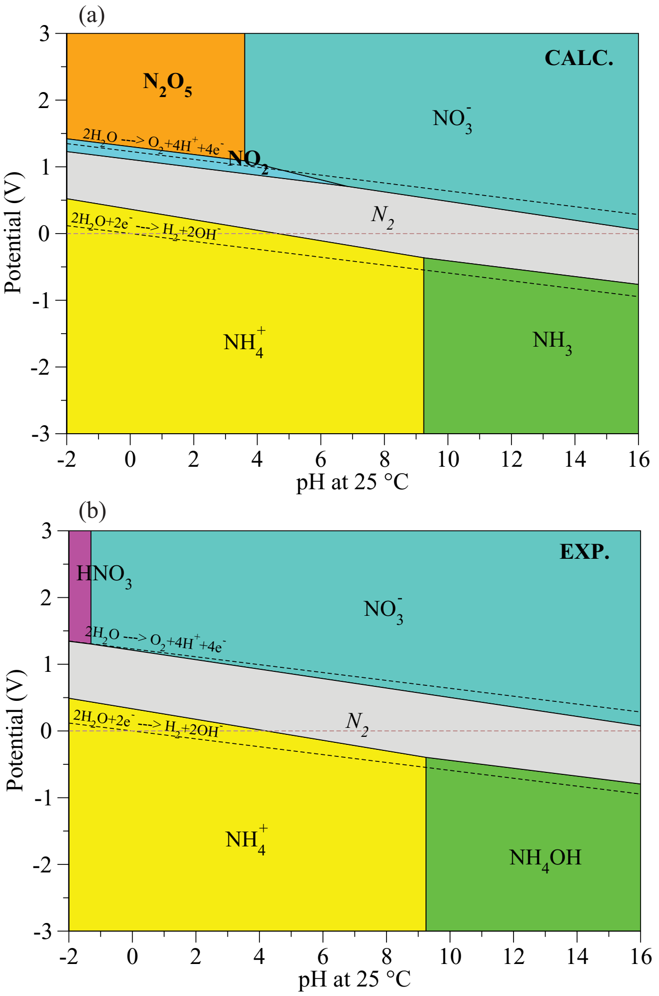

FIG. 5. (Color online) N Pourbaix diagrams generated using 10^{-6} M concentration for aqueous species at 25 °C. The diagram in (a) is calculated using the described formalism and (b) using only experimental data from Refs. 8–10.

Typically, water splitting is performed using two different materials: a metal for the hydrogen evolution and an oxide where the oxygen evolution takes place. However, ideally both reactions should take place in the same material, which would enable extracting oxygen and hydrogen gas simultaneously. This requires the material to be stable in the entire range of potentials between its VBM and CBM (given that they are outside the oxygen and hydrogen evolution reaction lines) for a certain pH. In Fig. 3, we show the Ti Pourbaix diagram from Sec. III together with the experimentally determined positions of the CBM and VBM (VBM is determined from the CBM level and band-gap value).[25] From this diagram, together with the band positions, we find that TiO_2 is stable at the conditions relevant for water-splitting activity for any pH value, in agreement with experimental findings. Equivalent analysis of the catalyst material stability can be performed in water under light illumination by comparing the CBM and VBM levels with absolute redox levels.[26]

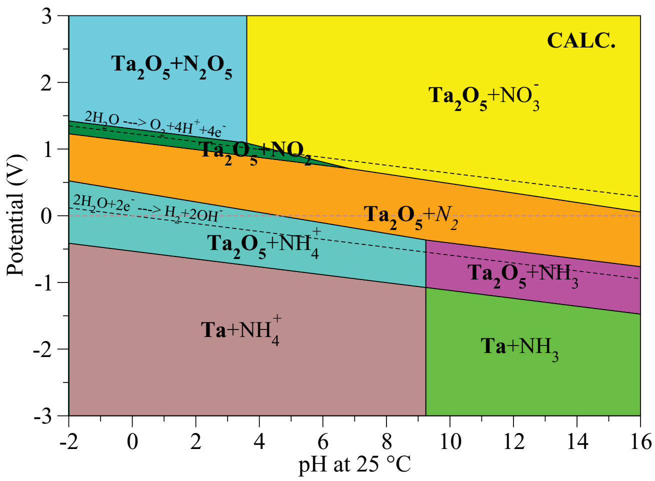

FIG. 6. (Color online) Pourbaix diagram for Ta_3N_5 generated using the formalism at 10^{-6} M concentration for aqueous species at 25 °C.

As mentioned, nitrides are known to be less stable in water, compared to oxides. Furthermore, for water-splitting applications, we require the catalyst material to be stable at the water-splitting activity potential, which for the nitrides is at lower potential than for oxides. To illustrate this, we have chosen Ta_3N_5, which has been suggested as an interesting water-splitting material.[27] In Fig. 6, we show the calculated Pourbaix diagram of the binary bulk compound Ta_3N_5, which (despite the excellent stability of Ta in water shown in Sec. III) exhibits no region of stability in water under any conditions, in agreement with experimental observations. Efforts in the oxynitride space[28] may prove more fruitful and generate materials which are more efficient in capturing the solar spectrum than oxides and more stable in water than pure nitrides.

B. Pt nanoparticle stability at low pH

There has been considerable indirect measurement and speculation on the electrochemical stability of small metal particles in catalytic arrays.[29,30] While basic thermodynamic theory (Gibbs-Thompson) predicts that particle stability decreases with size, there have been several measurements pointing to the opposite (see, for example, Ref. 31). Directly pertaining to this issue is the stability of Pt and Pt alloy catalysts in fuel-cell architectures. In the following section, we show how our formalism can be used to predict Pt nanoparticle stability in equilibrium with water under highly acidic conditions. The results of this work were previously published together with experimental validation through Scanning Tunneling Microscopy measurements in Ref. 32. In this section, we are focusing on explaining the formalism behind the calculated nanoparticle Pourbaix diagram.

We performed computations on more than 50 Pt nanoparticles of radius 0.25, 0.5, and 1 nm using the cuboctahedron shape of the nanoparticle as it is the experimentally observed surface structure for Pt particles <3.5 nm.[33] In water, these nanoparticles can take up species from the aqueous solution as adsorbants. The relevant free energy to equilibrate such an open system is a grand canonical potential, which is a Legendre transform of the Gibbs free energy:

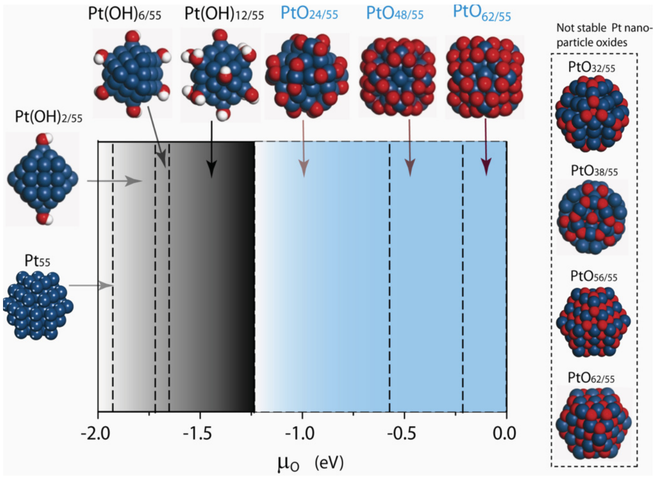

FIG. 7. (Color online) The calculated stable sequence of Pt nanoparticle phases as a function of oxygen chemical potential. The right-hand-side inset shows considered Pt oxide nanoparticles, which were not stable at these conditions.

$$\mu_{\mathrm{PtOxHy}} = E^{\mathrm{DFT}}_{\mathrm{PtO}_x\mathrm{H}_y} - x\mu_{\mathrm{O}} - y\mu_{\mathrm{H.}} \tag{67}$$

When O and H are in equilibrium with water, the relation $\mu_{H_2O} = \frac{1}{2}\mu_{O_2} + \mu_{H_2}$ holds and there is only one independent chemical potential as the chemical potential of H_2O, being the solvent, is set to a fixed value (see Sec. II D). We calculated all nanoparticles with different degrees and sites of absorbed oxygen and hydroxyl ions. Different Pt oxide nanoparticles were also calculated to investigate subsurface oxidation. For each configuration and coverage, the lowest energy state was selected. In this study, entropic effects were neglected for all phases considered. Figure 7 shows the result, which is an evolution of stable nanoparticle phases from dilute hydroxyl coverage to fully surface oxidized, as a function of oxygen chemical potential. Under the oxygen chemical potentials considered here, complete subsurface oxidization was never found to be favorable.

The above treatment allows for O and H species to exchange between the solution and the nanoparticle, but not Pt. In order to look at Pt dissolution, one can further Legendre transform with respect to the Pt chemical potential that is established in solution when Pt is dissolved at a certain concentration (e.g., typically taken as 1 M). Under acid conditions, there is only one aqueous species in the Pt-water phase diagram: $\mathrm{Pt}^{2+}_{(\mathrm{aq})}$. As outlined in Sec. II G, we incorporate that species by referencing it to a calculated solid phase. Bulk platinum oxide PtO was chosen as the solid reference state as it represents the most common valence state of Pt and is therefore likely to provide the most reliable experimental thermodynamic data of any Pt oxide/hydroxide solid phase. Following the structure outlined in Sec. II G, we obtain

$$\mu^{0}_{\mathrm{Pt}^{2+}(\mathrm{aq})} = \mu^{0,\mathrm{exp}}_{\mathrm{Pt}^{2+}(\mathrm{aq})} + \Delta\mu^{0,\mathrm{DFT-exp}}_{\mathrm{PtO}} \tag{68}$$

$$= -2.64 + [-0.66 - 1.17] \tag{69}$$

$$= -3.14\ \mathrm{eV}/\mathrm{Pt}^{2+}_{(\mathrm{aq})}. \tag{70}$$

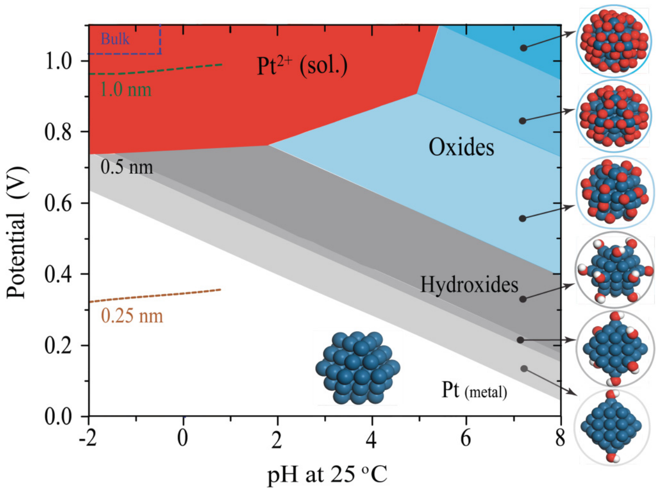

FIG. 8. (Color online) *Ab initio* calculated Pourbaix diagram for a Pt particle with radius 0.5 nm. The stability region of Pt^{2+} in solution is shown in red. The regions of hydroxide and oxygen surface adsorption are, respectively, in gray and blue. The green dashed line at 0.93 V show the solubility boundary at $[Pt^{2+}] = 10^{-6}$ M for a 1 nm Pt particle and the orange dashed line at 0.32 V for a 0.25 nm Pt particle.

It is worth noting from Eq. (70) that the discrepancy between the experimental formation enthalpy for solid PtO (Ref. 34) (-0.66 eV/fu) in the PtS structure and the corresponding DFT-derived value (-1.17 eV/fu) is 0.510 eV. Thus, in contrast to, e.g., Li^+ (see Sec. II G), the correction to chemical potential of the aqueous ion is quite significant in the case of Pt^{2+}. Without the referencing scheme in Sec. II G, the prediction of dissolution potentials for Pt in water using calculated solids would at best reproduce trends but not be quantitatively accurate.

Using the calculated nanoparticles and the aqueous state, we were able to construct a nanophase stability map as a function of pH and potential, i.e., a nanoparticle Pourbaix diagram (see Fig. 8). The gray (blue) areas in Fig. 8 indicate the region of OH^- and O^{2-} adsorption on the particle surface and the specific stable configurations are shown on the right-hand side of the figure. As seen in the figure, the 0.5-nm particle undergoes a small amount of hydroxyl adsorption (gray region) at low potential and pH, which crosses over into oxygen adsorption (blue region) as the potential and pH increase. The red area shows the region of stable Pt^{2+} dissolution (assuming a concentration of $Pt^{2+} = 10^{-6}$ M). Clearly, this region is extended compared to that of bulk Pt (blue dashed line), signifying a radical increase in dissolution tendency for nanoparticle Pt as compared to bulk. At the dissolution boundary, there is very little hydroxyl or oxygen adsorption, and consequently we observe that no significant passivation of the particle occurs which renders the dissolution potential almost independent of pH (for $pH < 2$). Similar behavior is observed for the 1-nm (green dashed line) and 0.25-nm particle (orange dashed line). For a 0.5-nm-radius Pt nanoparticle, the Pt/10^{-6} M Pt^{2+} boundary occurs at 0.7 V, while for 1-nm nanoparticles it is predicted to be 0.93 V, signifying decreased stability with decreasing particle size.

C. $LiFePO_4$ particle morphology as a function of pH and potential

Particle morphology control of advanced functional materials has applications in various fields, e.g., catalysis, electronics, and batteries.[35–38] In this context, material synthesis in an aqueous environment[39–44] is of particular interest as aqueous growth of materials offers several control parameters, such as the temperature, the pH, or the concentration of dissolved ions. For example, species in solution can bind to crystal facets and affect the relative surface energies, and hence the concentration of these species can be used to tailor crystal shape. In the following example, we investigate the equilibrium crystal shape of $LiFePO_4$, which is an important cathode material in the Li-ion battery field, as a function of solution conditions (represented by pH and electric potential). According to previous computational and experimental studies,[45–47] Li diffusion in the olivine structure $LiMPO_4$ is one dimensional along the [010] direction of the orthorhombic lattice (space group *Pnma*). Hence, maximal exposure of that facet and reduction of the thickness along this direction is expected to lead to improved kinetics.

Relevant surfaces for $LiFePO_4$ were calculated (see Ref. 48 for details), considering four chemical groups as potential adsorbates in an aqueous environment: hydrogen (H^+), water molecule (H_2O), hydroxyls (OH^-), and oxygen (O^{2-}). We only studied $LiFePO_4$ surfaces with one-monolayer adsorption for each species, and did not investigate any particular surface-structure patterns formed due to the variation in adsorbate concentrations. Detailed description of the calculations is being published elsewhere.[49]

The chemical potentials of H, O, and H_2O were worked out in Sec. II, and, at thermodynamic equilibrium, the chemical potential of OH is the sum of μ_H and μ_O: $\mu_{OH} = \mu_H + \mu_O = \mu_{H_2O} + \frac{1}{2}\mu_O$. Thus, all adsorbates are dependent on the oxygen chemical potential, and we can evaluate the grand potential for the different surfaces covered by each type of adsorbate as a function of the oxygen chemical potential. For every crystal facet, the surface adsorption with lowest value in surface grand potential is used as the equilibrium surface energy in the construction of Wulff shape. We also consider the possibility of Li^+ dissolving from $LiFePO_4$ surfaces into solution as Li is extremely unstable in water with its dissolution into aqueous Li^+ occurring at potentials as low as -3.0 V.[10] In principle, more species than Li can dissolve, but here we limit the investigation to the most soluble element present in the compound. The dissolution of Li^+ from $LiFePO_4$ surfaces into aqueous Li^+ can be summarized by the following reaction:

$$LiFePO_{4(s)} \rightarrow Li_{1-x}FePO_4(s) + xLi^+_{(aq)} + xe^-, \qquad (71)$$

where the solid phases can represent both bulk phases and surfaces of a $LiFePO_4$ crystal. We calculate the Gibbs free energy for Eq. (72) using the formation energies of the relevant solid and aqueous phases:

$$\Delta g = g_{Li_{1-x}FePO_4} - g_{LiFePO_4} - x g_{Li^+} - xEF, \qquad (72)$$

where E is the standard hydrogen potential, F is Faraday's constant, and the Gibbs free energy for Li^+ in solution is given by Eq. (59), and the Gibbs free energies for the solid phases are approximated by enthalpies calculated by first principles,

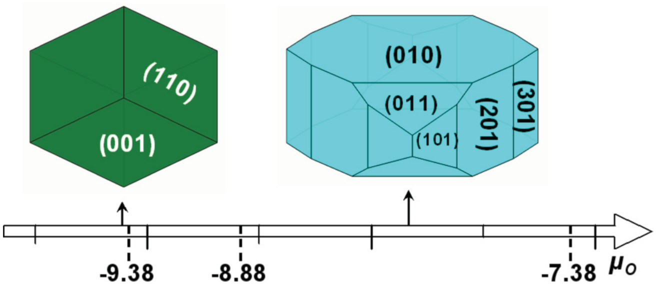

FIG. 9. (Color online) The particle morphology evolution for low oxygen chemical potentials. A green facet indicates surface coverage by H and blue indicates H_2O adsorption.

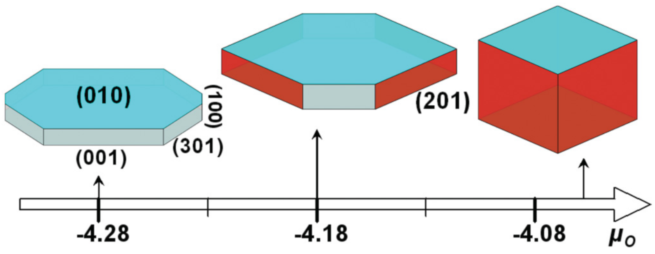

FIG. 10. (Color online) The particle morphology evolution for higher oxygen chemical potentials. Blue facets indicate surfaces covered by H_2O, gray ones are covered by OH, and red ones are covered by O molecule.

as described in Sec. II. If the Gibbs free energy in Eq. (72) is negative for a certain surface facet, that will change its surface energy and cause corresponding changes in the Wulff shape.

By varying the oxygen chemical potential, we simulate the appearance of different surface adsorbates on crystal surfaces, and investigate how the equilibrium particle shape changes as a function of the chemical environment. Figures 9 and 10 show the evolution of particle morphology as a function of oxygen chemical potential. We find that most surfaces are hydrogenated at very low oxygen chemical potential, which favors a diamond-shaped particle. Plate-type $LiFePO_4$ crystals with a large portion of (010) surface can be expected at relatively neutral aqueous condition where all facets are covered by water molecules. Between oxygen chemical potentials of −7.38 and −4.28 eV per O, we also observe that Li^+ ions start to dissolve from some H_2O-capped $LiFePO_4$ surfaces, which favor the (010) facet at lower pH, in agreement with experimental findings.[43] Optimizing for the (010) surface energy, we find that the Li dissolution at $\mu_O = -5.8$ eV and pH = 8.1 gives rise to a very thin platelike particle, which is highly interesting for reducing the Li diffusion length inside the particle. As the oxygen chemical potential is increased, the particle surfaces are gradually oxidized to OH and further to O adsorption, which favors more columnar particle shapes, as seen in Fig. 10. In conclusion, we find that the equilibrium particle shape of $LiFePO_4$ strongly depends on external chemical conditions relating to the anisotropic oxidation/reduction behavior of its surfaces, which in turn can be used to tune the particle shape as a function of aqueous synthesis conditions.

V. SUMMARY

In this paper, we present an efficient scheme for combining *ab initio* calculated solid states with experimental aqueous states through a framework of consistent reference energies. The accuracy of the methodology relies on two simple facts: (1) ions in a dissolved state are always the same, irrespective of whether they come from a surface or a nanoparticle, and (2) solid-state errors in DFT tend to be systematic and will to a large degree cancel between phases within the same chemistry. We show the methodology successfully applied to bulk Mn, Zn, Ta, Ti, and N as well as to (1) analyzing stability against dissolution for a Ta-N photocatalytic material, (2) predicting corrosion of nanoparticle Pt in acid, and (3) optimizing particle morphology evolution of $LiFePO_4$ under aqueous conditions. We hope that our work will enable efficient and accurate prediction of solid phase stability in equilibrium with water, which has many important application areas, such as corrosion, catalysis, and energy storage.

ACKNOWLEDGMENTS

Work at the Lawrence Berkeley National Laboratory was supported by the Assistant Secretary for Energy Efficiency and Renewable Energy, Office of Vehicle Technologies of the US Department of Energy, under Contract No. DEAC02-05CH11231. Work at the Massachusetts Institute of Technology was supported under Grant No. DE-FG02-96ER45571.

---

[1] S. Amira, D. Spångberg, and K. Hermansson, J. Chem. Phys. **124**, 104501 (2006).

[2] A. Pasquarello, I. Petri, P. S. Salmon, O. Parisel, R. Car, E. Toth, D. H. Powell, H. E. Fischer, L. Helm, and A. Merbach, Science **291**, 856 (2001).

[3] R. Benedek and M. M. Thackeray, Electrochem. Solid State Lett. A **9**, 265 (2006).

[4] R. B. R. and A. V. D. Walle, J. Electrochem. Soc. A **155**, 711 (2008).

[5] R. Benedek, M. M. Thackeray, and A. v. d. Walle, J. Electrochem. Soc. **20**, 369 (2010).

[6] Y. Marcus, J. Chem. Soc., Faraday Trans. **87**, 2995 (1991).

[7] L. Wang, T. Maxisch, and G. Ceder, Phys. Rev. B **73**, 195107 (2006).

[8] O. Kubaschewskii, C. B. Alcock, and P. J. Spencer, *Materials Thermochemistry*, 6th ed. (Pergamon, New York, 1992).

[9] J. W. Johnson, O. E. H., and H. H. C., Comput. Geosci. **18**, 899 (1992).

[10] M. Pourbaix, *Atlas of Electrochemical Equilibria in Aqueous Solutions* (National Association of Corrosion Engineers, Houston, Texas, 1974).

[11] G. Kresse and J. Furthmüller, Comput. Mater. Sci. **6**, 15 (1996).

[12] J. P. Perdew, K. Burke, and M. Ernzerhof, Phys. Rev. Lett. **77**, 3865 (1996).

[13] P. E. Blochl, Phys. Rev. B **50**, 17953 (1994).
[14] A. Jain, G. Hautier, S. P. Ong, C. J. Moore, C. C. Fischer, K. A. Persson, and G. Ceder, Phys. Rev. B **84**, 045115 (2011).
[15] R. O. Jones and O. Gunnarsson, Rev. Mod. Phys. **61**, 689 (1989).
[16] B. Hammer, L. B. Hansen, and J. K. Norskov, Phys. Rev. B **59**, 7413 (1999).
[17] J. X. Zheng, G. Ceder, T. Maxisch, W. K. Chim, and W. K. Choi, Phys. Rev. B **75**, 104112 (2007).
[18] W. Donner, C. Chen, M. Liu, A. J. Jacobson, Y.-L. Lee, M. Gadre, and D. Morgan, Chem. Mater. **23**, 984 (2011).
[19] P. K. Sharma and M. S. Whittingham, Mater. Lett. **48**, 319 (2001).
[20] I. I. Kornilov, V. V. Vavilova, L. E. Fykin, R. P. Ozerov, V. P. Solowiev, and S. P. Smirnov, Metall. Mater. Trans. B **1**, 2569 (1970).
[21] S.-H. Hong and S. A. sbrink, Acta Crystallogr. B **38**, 2570 (1982).
[22] D. Watanabe, O. Terasaki, A. Jostsons, and J. R. Castles, J. Phys. Soc. Jpn. **25**, 292 (1968).
[23] J. O. Hill, I. G. Worsley, and L. G. Hepler, Chem. Rev. **71**, 127 (1971).
[24] I. I. Zakharov, A. I. Kolbasin, O. I. Zakharova, I. V. Kravchenko, and V. I. Dyshlovoi, Theor. Exp. Chem. **43**, 66 (2007).
[25] A. J. Nozik and R. Mamming, J. Phys. Chem. **100**, 13061 (1996).
[26] H. Gerischer, J. Electroanal. Chem **82**, 133 (1977).
[27] M. Tabata, K. Maeda, M. Higashi, D. Lu, T. Takata, R. Abe, and K. Domen, Langmuir **26**, 9161 (2010).
[28] E. I. Castelli, T. Olsen, S. Datta, D. D. Landis, S. Dahl, K. S. Thygesen, and K. W. Jacobsen, Energy Environ. Sci. (to be published).
[29] Y. Shao-Horn, W. C. Sheng, S. Chen, P. J. Ferreira, E. F. Holby, and D. Morgan, Top. Catal. **46**, 285 (2007).
[30] J. Zhang, K. Sasaki, E. Sutter, and R. R. Adzic, Science **315**, 220 (2007).
[31] D. M. Kolb, G. E. Engelmann, and J. C. Ziegler, Angew. Chem., Int. Ed. **39**, 1123 (2000).
[32] L. Tang, B. Han, K. Persson, C. Friesen, T. He, K. Sieradzki, and G. Ceder, J. Am. Chem. Soc. **132**, 596 (2010).
[33] M. L. Sattler and P. N. Ross, Ultramicroscopy **20**, 21 (1986).
[34] D. C. Sassani and E. L. Shock, Geochim. Cosmochim. Acta **62**, 1643 (1998).
[35] I. Lee, F. Delbecq, R. Morales, M. A. Albiter, and F. Zaera, Nat. Mater. **8**, 132 (2009).
[36] N. Tian, Z. Y. Zhou, S. G. Sun, Y. Ding, and Z. L. Wang, Science **316**, 732 (2007).
[37] M. Graetzel, Nature (London) **414**, 338 (2001).
[38] P. Liu, S. H. Lee, C. E. Tracy, Y. Yan, and J. A. Turner, Adv. Mater. **18**, 2807 (2001).
[39] S. Kinge, T. Gang, W. J. M. Naber, H. Boschker, G. Rijnders, D. N. Reinhoudt, and W. G. van der Wiel, Nano Lett. **9**, 3220 (2009).
[40] Y. Dai, C. M. Cobley, J. Zeng, Y. Sun, and Y. Xia, Nano Lett. **9**, 2455 (2009).
[41] S. F. Yang, P. Y. Zavalij, and M. S. Whittingham, Electrochem. Commun. **3**, 505 (2001).
[42] S. Franger, F. Le Cras, C. Bourbon, and H. Rouault, Electrochem. Solid State Lett. A **5**, 231 (2002).
[43] K. Dokko, S. Koizumi, and K. Kanamura, Chem. Lett. **35**, 338 (2006).
[44] C. Delacourt, P. Poizot, S. Levasseur, and C. Masquelier, Electrochem. Solid State Lett. **9**, A352 (2006).
[45] D. Morgan, A. V. der Ven, and G. Ceder, Electrochem. Solid State Lett. A **7**, 30 (2004).
[46] M. S. Islam, D. J. Driscoll, C. A. J. Fisher, and P. R. Slater, Chem. Mater. **17**, 5085 (2005).
[47] K. Amine, J. Liu, and I. Belharouak, Electrochem. Commun. **7**, 669 (2005).
[48] L. Wang, F. Zhou, Y. S. Meng, and G. Ceder, Phys. Rev. B **76**, 165435 (2007).
[49] L. Wang, K. Persson, and G. Ceder (unpublished).